

# Sub-diffraction, Volume-confined Polaritons in the Natural Hyperbolic Material, Hexagonal Boron Nitride

Joshua D. Caldwell<sup>1</sup>, Andrey Kretinin<sup>2</sup>, Yiguo Chen<sup>3,6</sup>,  
Vincenzo Giannini<sup>3</sup>, Michael M. Fogler<sup>4</sup>, Yan Francescato<sup>3</sup>, Chase T. Ellis<sup>5</sup>, Joseph G.  
Tischler<sup>1</sup>, Colin R. Woods<sup>2</sup>, Alexander J. Giles<sup>5</sup>, Minghui Hong<sup>6</sup>, Kenji Watanabe,<sup>7</sup>  
Takashi Taniguchi,<sup>7</sup> Stefan A. Maier<sup>3</sup> and Kostya S. Novoselov<sup>2</sup>

<sup>1</sup> U.S. Naval Research Laboratory, 4555 Overlook Ave, S.W., Washington, D.C. USA

<sup>2</sup> School of Physics and Astronomy, University of Manchester, Oxford Rd, Manchester, United Kingdom

<sup>3</sup> The Blackett Laboratory, Imperial College London, London, United Kingdom

<sup>4</sup> Department of Physics, University of California San Diego, 9500 Gilman Dr, La Jolla, CA USA

<sup>5</sup> NRC Postdoctoral Fellow (residing at NRL, Washington, D.C.)

<sup>6</sup> Electrical and Computer Engineering, National University of Singapore, Singapore

<sup>7</sup> National Institute for Materials Science, 1-1 Namiki, Tsukuba, Ibaraki 305-0044, Japan

\*corresponding author, E-mail: [joshua.caldwell@nrl.navy.mil](mailto:joshua.caldwell@nrl.navy.mil)

**Hyperbolicity, an ability to simultaneously support metallic and dielectric optical response along orthogonal optical axes, was thought to occur only in metamaterials.<sup>1</sup> Recently, hexagonal boron nitride (hBN) was identified as a *natural hyperbolic material* (NHM).<sup>2</sup> In this Letter, we exploit the NHM response of hBN within periodic arrays of conical hBN nanoresonators to demonstrate ‘hyperbolic polaritons,’ deeply sub-diffraction guided waves that propagate through the volume rather than on the surface of a hyperbolic material. These polaritons are manifested as a series of resonances in two distinct spectral bands, with reciprocal dependences upon incident light polarization, modal order, and aspect ratio. The resonances exhibit unprecedented optical confinement<sup>3</sup> up to  $\lambda/86$  and record-high quality factors<sup>4,5</sup>  $Q$  up to 235 for sub-diffraction modes. These observations represent the first foray into creating NHM<sup>2,6</sup> building blocks for mid-infrared to terahertz nanophotonic and metamaterial devices.<sup>7</sup>**

Hyperbolic (or indefinite) materials --- where the principal components of the dielectric tensor have opposite signs --- have recently attracted much attention.<sup>1,8-13</sup> Unique properties and potential applications of hyperbolic media to nanolithography,<sup>14</sup> hyperlensing,<sup>15</sup> super-Planckian emission,<sup>16</sup> fluorescence engineering,<sup>17</sup> and nanophotonics<sup>1</sup> are enabled by sub-diffraction, guided modes or ‘hyperbolic polaritons’ (HP) that propagate within the volume material. These modes can have wavenumbers  $k$  that are arbitrarily large, i.e., modal confinement arbitrarily high, along with an extremely large optical density of states.<sup>1,10,13</sup> So far, HPs have not been fully demonstrated due to limitations of available materials. Previous experimental realizations of hyperbolic metamaterials (HMMs)<sup>3</sup> utilized metallic elements, and thus had the fundamental problem of plasmonic losses.<sup>4</sup> Another disadvantage of HMMs (built from alternating plasmonic and dielectric domains) is that the material axis with the negative real permittivity is rigidly fixed by the geometry, thus limiting design flexibility.

In contrast to HMMs, the hyperbolic behavior in NHMs is achieved within a homogeneous crystal, without the need for nanoscale plasmonic and dielectric domains or nanofabrication. In addition, as a van der Waals crystal,<sup>18</sup> hBN also offers monolayer thickness control and the capability to be transferred onto arbitrary substrates. NHMs still exhibit the open hyperbolic isofrequency surfaces of HMMs, rather than the closed elliptical surface associated with dielectric or metallic media.<sup>8,10,11,13</sup> Depending of the particular structure of the dielectric tensor, hyperbolicity can take one of two forms, Type I ( $\epsilon_z < 0; \epsilon_{x,y} > 0$ ) and Type II ( $\epsilon_z > 0; \epsilon_{x,y} < 0$ ), with the integer designating the number of principle axes with negative real permittivity. At large wavenumbers  $k$  such surfaces can be approximated by two cones with the apex angle defined by the ratio ( $\sqrt{\epsilon_{x,y}} / \sqrt{\epsilon_z} / i$ ). This implies that the HP waves are highly directional (i.e., at a given frequency they propagate at a fixed angle with respect to the  $z$ -axis) and can potentially have an extremely short wavelength, which is important for imaging and nanophotonic applications.

In hBN, both Type I and II behavior are observed simultaneously within two distinct spectral regimes. The corresponding frequency regions manifest themselves as high reflectivity (low transmission) in the FTIR spectra presented in Fig. 1 (a) for a 900 nm thick hBN flake on BaF<sub>2</sub>. These two regions are the lower (~12.1-13.2  $\mu\text{m}$ ) and upper (~6.2-7.3  $\mu\text{m}$ ) Reststrahlen bands of hBN that are found between the longitudinal (LO) and transverse optic (TO) phonon frequencies [Fig. 1 (a)].<sup>7,19</sup> The two bands are highlighted as the shaded regions in the derived real permittivity in Fig. 1 (b) for both the ordinary ( $\epsilon_{x,y}$ , green curve) and extraordinary ( $\epsilon_z$ , magenta curve) optical axes, with the corresponding isofrequency contours provided as Fig. 1 (c).

In order to probe high- $k$  HPs optically, one has to couple them to low- $k$  far-field radiation. Our solution is to work with hBN structures of finite size. Geometric quantization of HPs endows them with a finite dipole moment that leads to resonant features in optical reflectivity. Conical nanoresonators used for this purpose were fabricated from a series of hBN flakes with thicknesses from 80-410 nm on SiO<sub>2</sub>/Si or quartz substrates using electron beam lithography and reactive ion etching. An scanning electron microscope (SEM) image of a representative array is provided as an inset to Fig. 2 (a). The reflection spectra collected from a periodic array of 410 nm tall, 375 nm diameter hBN structures on a 600 nm pitch are presented for near-normal (red curve), ~25° off-normal (green curve) and ~70° grazing incidence (blue curve) excitations [see schematic in Fig. 2(b)]. Note, as conical nanoresonators have a varying diameter, all values are reported as the volume-preserved diameter (see Supplementary Materials). These spectra demonstrate a series of resonances within both the (Type II) upper and (Type I) lower Reststrahlen bands as shown in Fig. 2 (a) and (b), respectively. The corresponding finite element calculations are provided in Fig. 2 (c) and (d). They predict four sets of modes, two per Reststrahlen band. Within each band, the sets of resonances exhibit mutually orthogonal polarization selection rules; namely, the highest amplitude response is achieved in both

Reststrahlen bands when the electric field is parallel to the axis along which the real permittivity is negative.

In Fig. 3 (a) and (b) the calculated reflection spectra of the HPs for the upper and lower Reststrahlen bands at  $0^\circ$  and  $70^\circ$ , respectively, are compared with their counterparts for fictitious isotropic materials using either the ordinary [ $\epsilon_{x,y}$ , Fig. 3 (c)] or the extraordinary [ $\epsilon_z$ , Fig. 3 (d)] components of the permittivity. The surface plots of the electric field are provided as insets. From these calculations, one can see that the two isotropic cases result in surface-confined modes, consistent with surface phonon polariton (SPhP)<sup>5</sup> and plasmonic resonators.<sup>20</sup> However, the anisotropic, hyperbolic response leads to modes propagating within the *volume* of the material, with a ‘cross-hatch’ shaped  $E$ -field profile. While volume-confined optical modes are readily observed within dielectric resonators,<sup>21</sup> these systems are still governed by the diffraction limit. Therefore, the HPs discussed here demonstrate that sub-diffraction, volume-bound modes can be realized and potentially provide dramatic advancements for nanophotonic devices, such as the sub-diffraction equivalent of optical fibers. In addition, as both Type I and II hyperbolic behavior are observed in hBN, dual-band and/or polarization selective nanophotonic devices are also possible.

From the spatial distributions of the magnetic ( $H$ ) and electric ( $E$ ) near-fields [Fig. 4 (a) and (b)], the sets of higher amplitude modes within the upper [ $0^\circ$ , Fig. 2 (a)] and lower [ $70^\circ$ , Fig. 2 (b)] Reststrahlen bands can be classified as a series of higher order modes. This is demonstrated by the increasing number of  $H$  field oscillations observed along the  $z$ -axis. Interestingly, the resonances shift in opposite directions, as the Type II upper (Type I lower) Reststrahlen modes are found to shift to *lower* (higher) frequency with increasing modal order. This anomalous behavior was also reported for the first and second order modes from Type II Ag/Ge HMM resonators,<sup>22</sup> and the reciprocal nature of the Type I and II modes was recently predicted theoretically for higher order polaritons within thin flakes of hBN.<sup>2</sup> This reciprocal behavior occurs due to the inversion of the sign of the group velocity between the Type I lower and Type II upper Reststrahlen bands [see green arrows in isofrequency contours in Fig. 1(c)]. Furthermore, as both sets of modes are stimulated when the  $E$  field is aligned with the principle axis exhibiting negative real permittivity, the polarization selection rules are also inverted. Unlike in HMM structures, all resonances observed here had extremely narrow linewidths, on the order of  $6\text{-}23\text{ cm}^{-1}$  and  $3\text{-}5\text{ cm}^{-1}$  for the upper and lower Reststrahlen bands. This corresponds to  $Q=66\text{-}220$  and  $Q=140\text{-}235$ , respectively. In addition, the hyperbolic nature and low optical losses of the material enabled photon confinements in nanoresonators with heights  $17\text{-}86\times$  and diameters  $6\text{-}61\times$  smaller than the resonant wavelength. In principle, these modes can be supported down to the atomic-scale, as demonstrated by the SPhPs observed within monolayer hBN flakes<sup>2</sup> and nanotubes<sup>23</sup> via near-field optical microscopy, however, finite far-field extinction from our nanostructure arrays have thus far limited monolayer-thick resonators from being realized.

Currently, no description of the mode type has been applied to HPs that can differentiate between the two types of hyperbolicity, modal order and polarization requirements. Therefore based on the predominant series of modes within each spectral band being defined primarily by the  $H$  field component aligned along the positive permittivity optical axis [ $H_z$  for upper and  $H_x$  for lower Reststrahlen bands, see Supplemental Materials], we designate these modes as transverse magnetic (TM) variety. In order to delineate each of the modes, we designate each as  ${}^R TM_{ml}$ , with the  $z$ -axis angular momentum number  $m = 0$  or  $m = 1$  distinguishing modes stimulated with  $E$  aligned along or normal to this axis, respectively,  $l = 1, 2, 3, \dots$ , referring to the modal order, see Figs. 2 (c), 2 (d), and 4., and R corresponding to the upper (“U”) or lower (“L”) Reststrahlen bands. We have to this point only discussed the two series of modes with the highest amplitude in each Reststrahlen band ( ${}^L TM_{0l}; {}^U TM_{1l}^U$ ), however, as mentioned above, each band also has two sets of weaker resonances ( ${}^L TM_{1l}; {}^U TM_{0l}$ ). The weaker  ${}^L TM_{1l}$  modes are experimentally observed within the lower Reststrahlen band at normal incidence excitation [red curve, Fig. 2 (b)]. For clarity, the first three orders of these modes are designated with an “\*”. Due to the close spectral proximity of the  ${}^U TM_{1l}$  and  ${}^U TM_{0l}$ , along with the mixing of polarization components at  $70^\circ$  incidence, the weaker  ${}^U TM_{0l}$  could not be clearly assigned.

The guided nature of the HPs can be seen from the spatial color plots of the  $H$  (left column) and  $E$  (right column) near-field distributions for the series of stronger  ${}^U TM_{1l}$  [Fig. 4 (a)] and  ${}^L TM_{0l}$  [Fig. 4 (b)] modes, as well as in the videos of the time-variant  $H$  and  $E$  near-fields provided in the Supplementary Material. The strict directionality of the guided waves is manifested as the distinct ‘cross-hatch’ in  $E$ . The number of  $E$  field crossings increases by one with an equivalent increase in the modal order  $l$ . The resulting guided modes are manifested as resonances in the far-field reflection spectra [Fig. 2 (a) and (b)], when the standing wave condition  $\lambda_{res} = j\lambda_{HP} / 2$  is met, where  $j$  is an integer and  $\lambda_{HP}$  is the compressed modal wavelength of the hyperbolic polariton. As the HPs within the two Reststrahlen bands have group velocities of opposite signs, the angle of the cross-hatch patterns, and therefore the number of crossings, increase in opposite spectral directions, resulting in the reciprocal spectral shifts for higher order modes.

Additional insight into the structure of HP resonances is provided by the following analytical results. Unfortunately, no analytical theory for resonators of truncated cones is available. However, it exists for spheroidal particles (Supplementary Material).<sup>24</sup> It predicts that the resonant frequency for each HP mode depends primarily upon the aspect ratio (diameter/height), as demonstrated in the color plots presented in Figs. 5 (a) and (b), for the  ${}^U TM_{1l}$  and  ${}^L TM_{0l}$  resonances, respectively. The corresponding experimental aspect ratio dependences are superimposed as the various data points. The agreement between the experimental results and the calculations is impressive, especially when one considers the effect of the substrate is disregarded in these model calculations. The overall trends are reproduced by the totality of the

experimental data derived from 23 different periodic arrays with 6 different heights and 9 distinct diameters.

Our work constitutes the first experimental observation of the long-sought, sub-diffraction guided-waves, doing so using a NHM. Compared to similar efforts in artificial HMMs,<sup>22</sup> the results presented here demonstrated not only Type II but also Type I modes, therefore enabling the experimental demonstration of their reciprocal behavior. These observations, coupled with the ability to control the size of hBN resonators down to the atomic scale and the drastically reduced linewidths and modal wavelengths (i.e., deeper photonic confinement) demonstrate the potential of hBN and related van der Waals materials<sup>25</sup> for versatile nanophotonic and metamaterial applications and should extend the spectral range of NHMs from the mid-infrared to the single-digit terahertz. The volume-confinement of HPs coupled with the low optical losses of polar dielectric crystals such as hBN, promises disruptive technologies such as the nanoscale optical fibers, which when coupled with nanoscale resonators could enable nanophotonic circuits,<sup>26</sup> such as those desired for free-space communications in the mid-IR. The spectral overlap between the Reststrahlen bands of hBN with the vibrational modes of many chemical species of interest could also provide the basis for advances in molecular spectroscopy.<sup>27</sup> In addition, advancements in other metamaterial and nanophotonic applications such as flat optics,<sup>28</sup> super-resolution imaging,<sup>15</sup> and tailored thermal sources,<sup>29</sup> are also possible.

## Acknowledgements

Funding for NRL authors was provided by the NRL Nanoscience Institute. J.D.C. carried out this work through the NRL Long-Term Training (Sabbatical) Program at the University of Manchester. C.T.E. and A.J.G. acknowledges support from the NRC NRL Postdoctoral Fellowship Program. Y.F., S.M. and V.G. acknowledge support from EPSRC and Leverhulme Trust. C.R.W., A.K. and K.S.N. acknowledge support from the Engineering and Physical Sciences Research Council (UK), The Royal Society (UK), European Research Council and EC-FET European Graphene Flagship. J.D.C. would like to thank Dr. Jeremy Robinson of NRL for helpful discussions and comments.

## Methods

Hexagonal boron nitride (hBN) was exfoliated from hBN crystals grown via the high pressure/high temperature method<sup>30</sup> onto either 90 nm thick SiO<sub>2</sub> on doped *n*-type Silicon or quartz substrates using standard dicing tape. Using AFM, hBN flakes with thicknesses ranging from 60-410 nm and spatial sizes sufficient for nanostructure array patterning (>50 μm on a side), were identified. The array patterns were defined using electron beam lithography and were patterned into a bilayer PMMA resist, with nanostructures ranging from 100-1000 nm in diameter being fabricated, with the periodicity (center-to-center) being maintained at a 3:1 ratio with the designed top diameter. A 30 nm thick aluminum film was deposited using thermal evaporation for the standard liftoff procedure and the hBN nanostructures were defined by

reactive ion etching in an inductively coupled CHF<sub>3</sub>/O<sub>2</sub> plasma (Oxford Instruments PlasmaLab) at a pressure of 10 mTorr, resulting in an etch rate of ~1 μm/min. The RF power applied to the plasma reactor and the substrate was 200 W and 20 W, respectively. The CHF<sub>3</sub>/O<sub>2</sub> flow ratio (17.5 / 10 sccm) was optimized to increase the BN-to-SiO<sub>2</sub> selectivity. The etch rates of the aluminum hard mask and SiO<sub>2</sub> substrates were determined to be insufficient for any significant etching to occur within this time. The aluminum hard mask was then removed via a standard TMAH (MICROPOSIT<sup>®</sup> MF-319) wet chemical etchant.

Mid-IR reflectance measurements were undertaken using a Bruker Hyperion microscope coupled to a Bruker Vertex80v FTIR spectrometer. Three different objectives were used to obtain normal (ZnSe), off-normal (36x Cassegrain) and grazing (15x GAO) incidence spectra from the nanostructures. The spectra were collected with a 2 cm<sup>-1</sup> spectral resolution and spatial resolution defined by the internal adjustable aperture of the microscope that was set to the size of the specific array of interest. All measurements were performed in reference to a gold film.

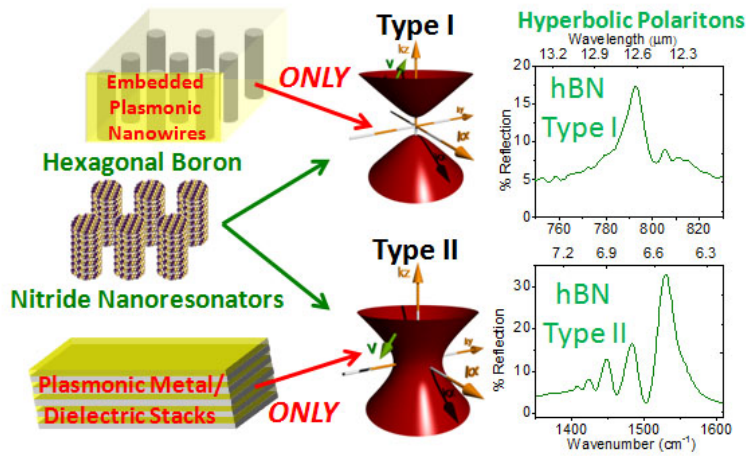
To better understand the deeply sub-diffraction HP modes involved in these nanostructures, full-wave 3D electrodynamic calculations using the RF module of the finite-element package COMSOL were performed. The anisotropic optical constants were extracted from the above mentioned method and the geometry of the experimental nanostructures was determined from atomic force microscopy and scanning electron microscopy. In an effort to closely match the experimental conditions, the simulations were undertaken using the incident optical field at 0°, 25° and 70° to match that of the ZnSe (0.08 NA), 36x Cassegrain (0.52 NA) and grazing incidence (GAO) objectives of the Bruker FTIR microscopes described above.

## References

- 1 Cortes, C. L., Newman, W., Molesky, S. & Jacob, Z. Quantum nanophotonics using hyperbolic metamaterials. *JOpt* **14**, 063001, (2012).
- 2 Dai, S. *et al.* Tunable phonon polaritons in atomically thin van der Waals crystals of boron nitride. *Science (Wash.)* **343**, 1125-1129, (2014).
- 3 Yang, X., Yao, J., Rho, J., Xiaobo, Y. & Zhang, X. Experimental realization of three-dimensional indefinite cavities at the nanoscale with anomalous scaling laws. *Nature Photonics* **6**, 450-453, (2012).
- 4 Khurgin, J. B. & Sun, G. Scaling of losses with size and wavelength in nanoplasmonics and metamaterials. *Appl. Phys. Lett.* **99**, 211106, (2011).
- 5 Caldwell, J. D. *et al.* Low-Loss, Extreme Sub-Diffraction Photon Confinement via Silicon Carbide Surface Phonon Polariton Nanopillar Resonators. *Nano Lett.* **13**, 3690-3697, (2013).
- 6 Sun, J., Litchinitser, N. M. & Zhou, J. Indefinite by Nature: From Ultraviolet to Terahertz. *ACS Photonics* **Articles ASAP**, (2014).
- 7 Caldwell, J. D. *et al.* Low-Loss, Infrared and Terahertz Nanophotonics with Surface Phonon Polaritons. *Nanophotonics* **submitted**, (2014).
- 8 Noginov, M., Lapine, M., Podolskiy, V. A. & Kivshar, Y. Focus issue: hyperbolic metamaterials. *Opt. Express* **21**, 14895-14897, (2013).
- 9 Argyropoulos, C., Estakhri, N. M., Monticone, F. & Alu, A. Negative refraction, gain and nonlinear effects in hyperbolic metamaterials. *Opt. Express* **21**, 15037-15047, (2013).

- 10 Guo, Y., Newman, W., Cortes, C. L. & Jacob, Z. Applications of Hyperbolic Metamaterial Substrates. *Advances in OptoElectronics* **2012**, 452502, (2012).
- 11 Poddubny, A., Iorsh, I., Belov, P. & Kivshar, Y. Hyperbolic metamaterials. *Nature Photonics* **7**, 958-967, (2013).
- 12 Drachev, V. P., Podolskiy, V. A. & Kildishev, A. V. Hyperbolic metamaterials: new physics behind a classical problem. *Opt. Express* **21**, 15048-15064, (2013).
- 13 Jacob, Z. *et al.* Engineering Photonic Density of States Using Metamaterials. *ApPPL* **100**, 215-218, (2010).
- 14 Xiong, Y., Liu, Z. & Zhang, X. A simple design of flat hyperlens for lithography and imaging with half-pitch resolution down to 20 nm. *Appl. Phys. Lett.* **94**, 203108, (2009).
- 15 Liu, Z., Lee, H., Xiong, Y., Sun, C. & Zhang, X. Far-field optical hyperlens magnifying sub-diffraction limited objects. *Science* **315**, 1686, (2007).
- 16 Guo, Y., Cortes, C. L., Molesky, S. & Jacob, Z. Broadband super-Planckian thermal emission from hyperbolic metamaterials. *Appl. Phys. Lett.* **101**, 131106, (2012).
- 17 Jacob, Z., Smolyaninov, I. I. & Narimanov, E. E. Broadband Purcell effect: Radiative decay engineering with metamaterials. *Appl. Phys. Lett.* **100**, 181105, (2012).
- 18 Geim, A. K. & Grigorieva, I. V. Van der Waals heterostructures. *Nature* **499**, (2013).
- 19 Hillenbrand, R., Taubner, T. & Keilmann, F. Phonon-enhanced light-matter interaction at the nanometre scale. *Nature* **418**, 159-162, (2002).
- 20 Maier, S. A. *Plasmonics: Fundamentals and Applications*. (2007).
- 21 Bezares, F. J. *et al.* Mie Resonance-Enhanced Light Absorption in Periodic Silicon Nanopillar Arrays. *Opt. Express* **21**, 27587-27601, (2013).
- 22 Yang, K. Y. *et al.* Subwavelength imaging with quantum metamaterials. *PhRvB* **86**, 075309, (2012).
- 23 Xu, X. G., Tanur, A. E. & Walker, G. C. Phase controlled homodyne infrared near-field microscopy and spectroscopy reveal inhomogeneity within and among individual boron nitride nanotubes. *J. Phys. Chem. A* **117**, 3348-3354, (2013).
- 24 Fonoberov, V. A. & Balandin, A. A. Polar optical phonons in wurtzite spheroidal quantum dots: theory and application to ZnO and ZnO/MgZnO nanostructures. *J. Phys.: Condens. Matter* **17**, 1085-1097, (2005).
- 25 Yu, N., A.K. & Capasso, F., I.V. Flat optics with designer metasurfaces Van der Waals heterostructures. *Nature* **13499**, 139-150, (20142013).
- 26 Engheta, N. Circuits with Light at Nanoscales: Optical Nanocircuits Inspired by Metamaterials. *Science (Wash.)* **317**, 1698-1702, (2007).
- 27 Anderson, M. S. Enhanced Infrared Absorption with Dielectric Nanoparticles. *Appl. Phys. Lett.* **83**, 2964-2966, (2003).
- 28 Yu, N. & Capasso, F. Flat optics with designer metasurfaces. *Nature Materials* **13**, 139-150, (2014).
- 29 Schuller, J. A., Taubner, T. & Brongersma, M. L. Optical antenna thermal emitters. *Nature Photonics* **3**, 658-661, (2009).
- 30 Watanabe, K., Taniguchi, T. & Kanda, H. Direct-bandgap properties and evidence for ultraviolet lasing of hexagonal boron nitride single crystal. *Nature Materials* **3**, 404-409, (2004).

**Figure Captions:**



**TOC Fig:** While plasmonic/dielectric hyperbolic metamaterials can only have one principle axis provide negative real permittivity, and thus, one type of hyperbolic behavior, the natural hyperbolic material hexagonal boron nitride, offers both types. This is due to the homogeneous nature of the crystal and the highly anisotropic crystal structure. By exploiting this, we demonstrate deeply sub-diffraction hyperbolic polaritons, which exhibit the nanoscale photonic confinement of guided waves that propagate through the volume of the material.

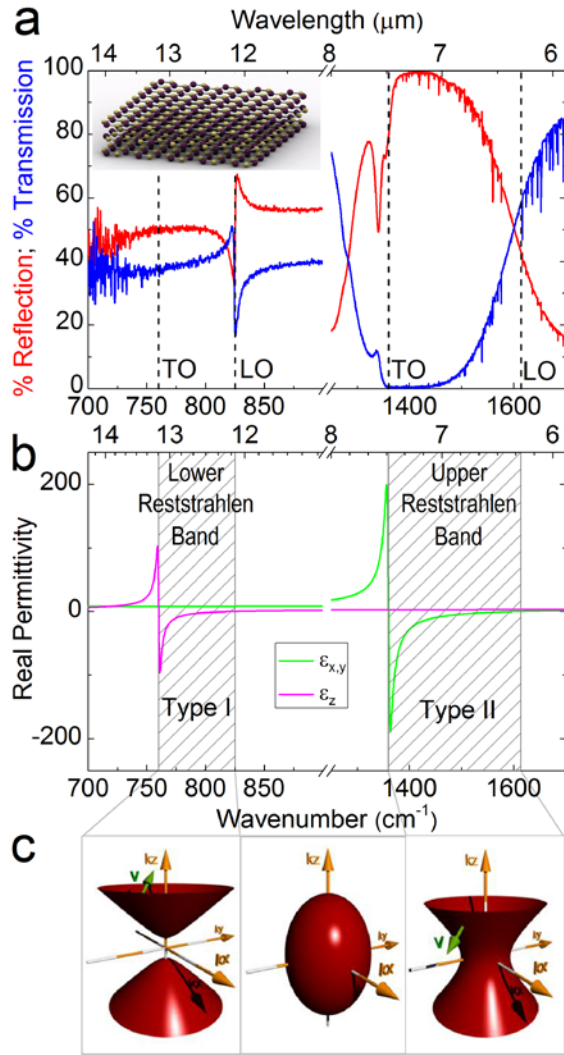


**Fig. 1:** (a) FTIR reflection (red curve) and transmission (blue curve) using a 36x Cassegrain objective from a 900 nm thick, hBN flake exfoliated onto a 500  $\mu\text{m}$  thick  $\text{BaF}_2$  substrate. The spectral positions of the transverse (TO) and longitudinal (LO) optic phonons of the two principle axes for hBN are provided by the vertical dashed lines, while a schematic of the hBN layered structure is presented as the inset. (b) Derived real permittivity from the hBN flake along the ordinary ( $\epsilon_{x,y}$ ) and extraordinary ( $\epsilon_z$ ) optical axes as labeled, the Type I lower and II upper Reststrahlen bands are labeled and highlighted by the shaded boxes. The corresponding isofrequency curves from the regions are provided as (c).

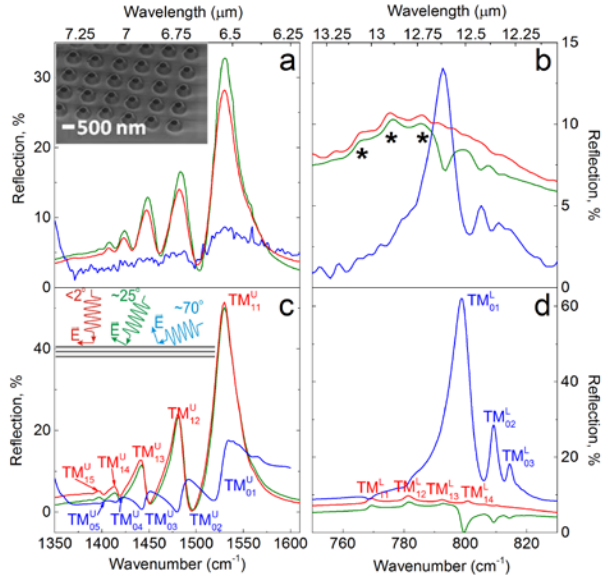


**Fig. 2:** FTIR reflection spectra of the (a) upper and (b) lower Reststrahlen bands collected from a periodic array (600 nm center-to-center pitch) of 375 nm volume-preserved diameter, 410 nm tall hBN conical nanoresonators. The spectra were collected using three different IR objectives giving rise to incident angles near-normal ( $< 2^\circ$ , red curve), off-normal ( $\sim 25^\circ$ , green curve) and at near-grazing incidence ( $\sim 70^\circ$ , blue curve). For clarity, the near-grazing incidence spectra is offset by -4% in (b). Corresponding spectra were calculated for both Reststrahlen bands using finite element methods in COMSOL and the spectra are provided in (c) and (d), respectively. The modal assignments are labeled in the figure according to the methodology described in the text. Inset: SEM image of a representative array of hBN nanoresonators.

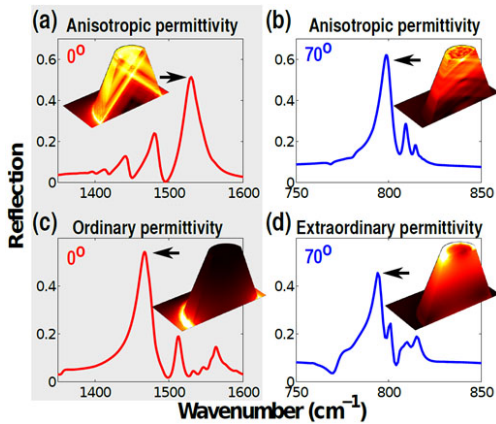


**Fig 3:** Simulated reflection spectra for the upper (left column) and lower (right column) Reststrahlen bands at  $0^\circ$  and  $70^\circ$  incident angles, respectively, using the hyperbolic anisotropic optical constants (top) and using fictional isotropic constants corresponding to the (c) ordinary and (d) extraordinary optical response. The spatial distributions of the  $|E|$  for the highest amplitude peak in each graph are provided as the inset.

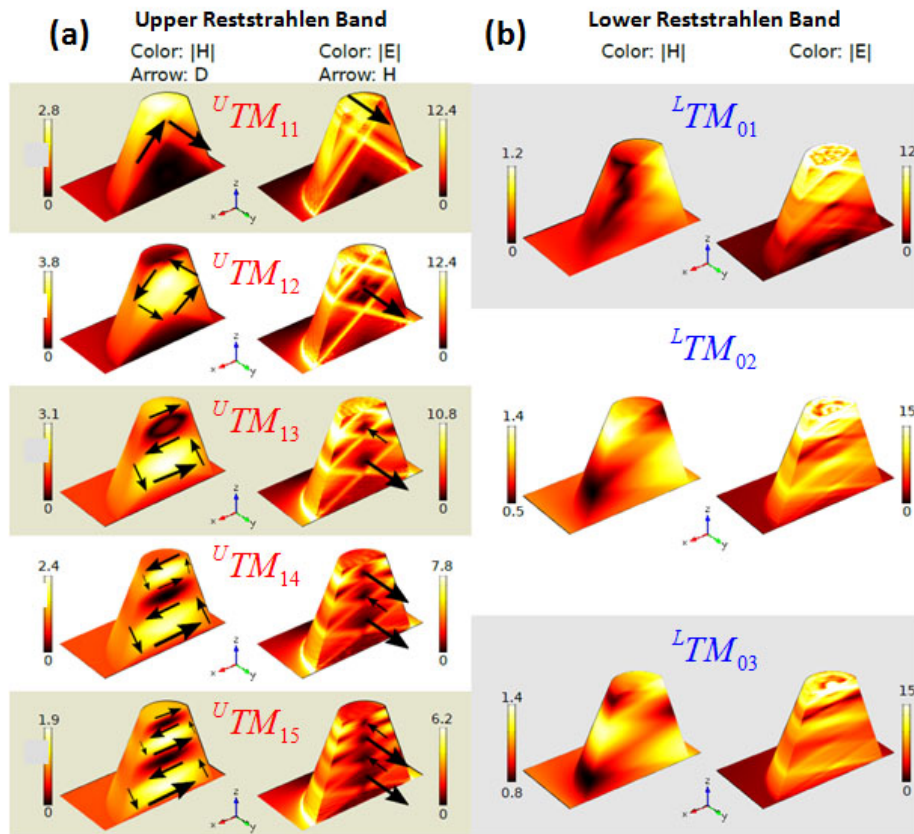


**Fig. 4:** Color surface plots of the magnetic (H, left column) and electric (E, right column) for each of the resonances modes observed within the (a) upper and (b) lower Reststrahlen bands at  $0^\circ$  and  $70^\circ$  incident angles, respectively. The assignments of the modes are provided in the figure and correspond to those shown in Fig. 2 (c) and (d). The black arrows in (a) present either the displacement current (D) or the magnetic field (H) vectors. The values reported in the color scale are the enhancements over the incident fields, which was set to a value of 1.

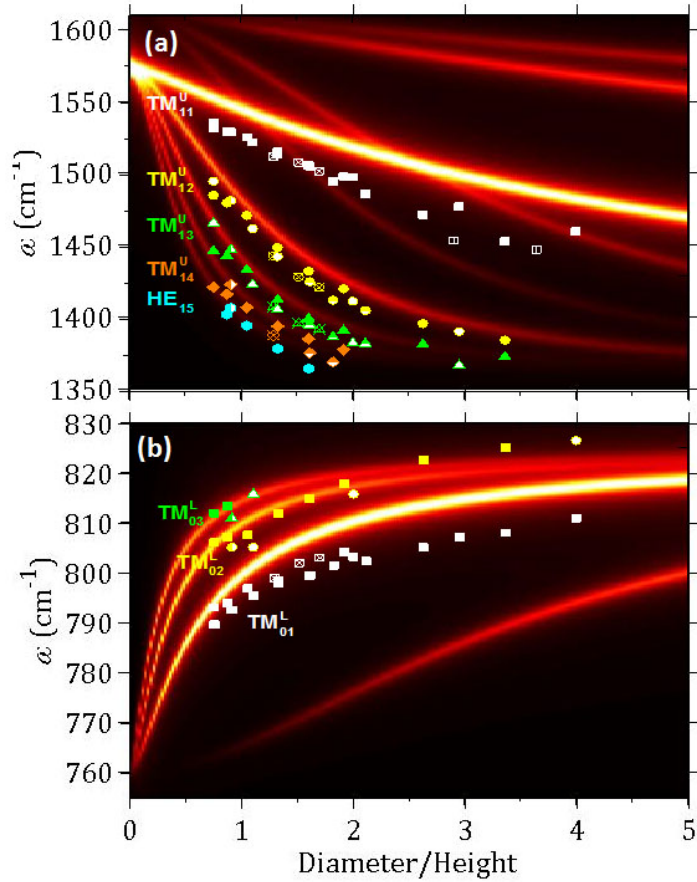


**Fig. 5:** Analytical calculation of the aspect ratio dependence of the resonant frequencies for ellipsoidal nanoresonators within the (a) upper and (b) lower Reststrahlen bands. For simplicity, only the  ${}^U TM_{l_l}$  and  ${}^L TM_{0_l}$  modes are provided. The corresponding experimental resonance positions for the hBN conical nanoresonators are superimposed onto these plots. The various symbols refer to arrays with different nanoresonator heights. In all, the experimental data represent the results from 23 different arrays with varying heights and diameters.